

Supplemental Information for Plurality of excitons in Ruddlesden-Popper metal halides and the role of B-site metal cation

Giulia Folpini,[†] Maurizia Palumbo,^{*,‡} Daniele Cortecchia,[†] Luca Moretti,[¶] Giulio
Cerullo,[¶] Annamaria Petrozza,[†] Giacomo Giorgi,^{*,§,||,⊥} and Ajay Ram Srimath
Kandada^{*,#}

[†]*CNST@Polimi, Istituto Italiano di Tecnologia,
Via Pascoli 70/3, Milano, Italy.*

[‡]*Dipartimento di Fisica and INFN, Università di Roma "Tor Vergata",
Via della Ricerca Scientifica 1 Roma, Italy*

[¶]*Dipartimento di Fisica, Politecnico di Milano,
Piazza Leonardo da Vinci 32, Milano, Italy.*

[§]*Department of Civil and Environmental Engineering (DICA), University of Perugia,
Via G. Duranti, 93 - 06125 - Perugia, Italy*

^{||}*CIRIAF - Interuniversity Research Centre, University of Perugia, Via G. Duranti 93,
06125 Perugia, Italy.*

[⊥]*CNR-SCITEC, I-06123, Perugia, Italy.*

[#]*Department of Physics and Center for Functional Materials, Wake Forest University,
Winston-Salem (N.C), United States*

E-mail: maurizia.palumbo@roma2.infn.it; giacomo.giorgi@unipg.it; srimatar@wfu.edu

Computational Details

The initial atomic structures have been extracted by experimental X-rays data directly taken from the paper of Zhang et al.¹ and Sheikh et al.² for the stacked and single layer structure of tin based systems, respectively. On the other hand, both the stacked and the monolayer structure for the Pb-based systems are taken from the work of Du et al.³ Geometry optimizations were initially performed by means of the Density Functional Theory (DFT) as implemented in the VASP code.⁴⁻⁷ The Perdew-Burke-Ernzerhof (PBE) electron exchange-correlation functional was here employed⁸ along with the projector augmented wave (PAW) method.^{9,10} The cutoff energy for the plane-wave basis set was set to 600 eV while a $6 \times 6 \times 2$ Γ -centered mesh of the Brillouin zone was adopted. Calculations were considered converged when residual forces were lower than $0.02 \text{ eV}/\text{\AA}$. Starting from the experimentally reported structure of Zhang et al.¹ ($P\bar{1}$ (2) space group 12) we obtain an optimized structure described by such parameters: $a=8.573\text{\AA}$, $b=8.559\text{\AA}$, $c=32.188\text{\AA}$, $\alpha=89.50^\circ$, $\beta=89.565^\circ$, $\gamma=89.285^\circ$.

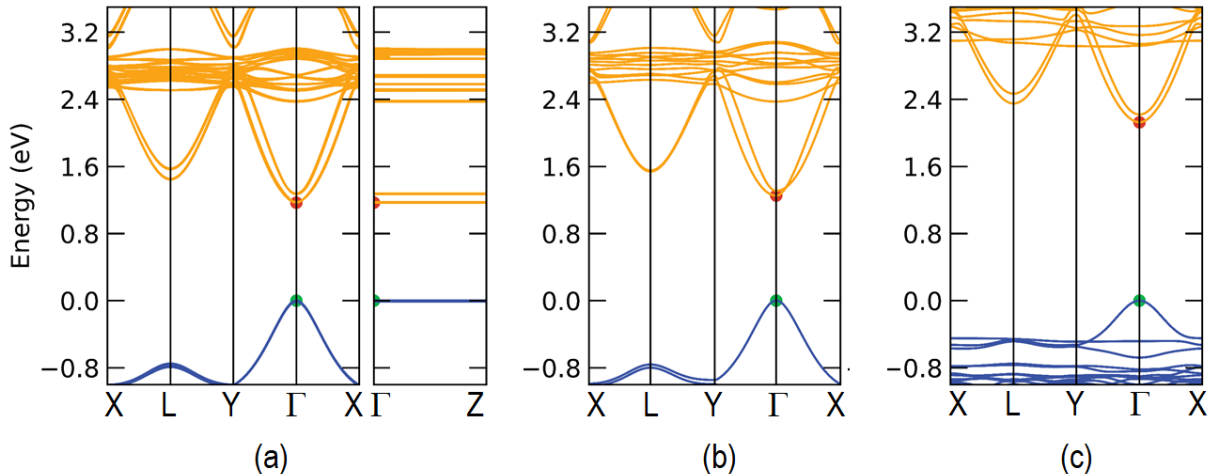


Figure S1: PAW/PBE-D3 calculated bandstructure (no SOC) for the (a) $(\text{PEA})_2\text{SnI}_4$ stacked structure, (b) $(\text{PEA})_2\text{SnI}_4$ monolayer, and for the (c) $(\text{PEA})_2\text{PbI}_4$ monolayer

As single-layer structure for $(\text{PEA})_2\text{SnI}_4$ we adopt and optimize the cell reported by Sheikh et al.² (still $P\bar{1}$ (2), space group 12) for which the PBE-D3 optimized values are: $a=$

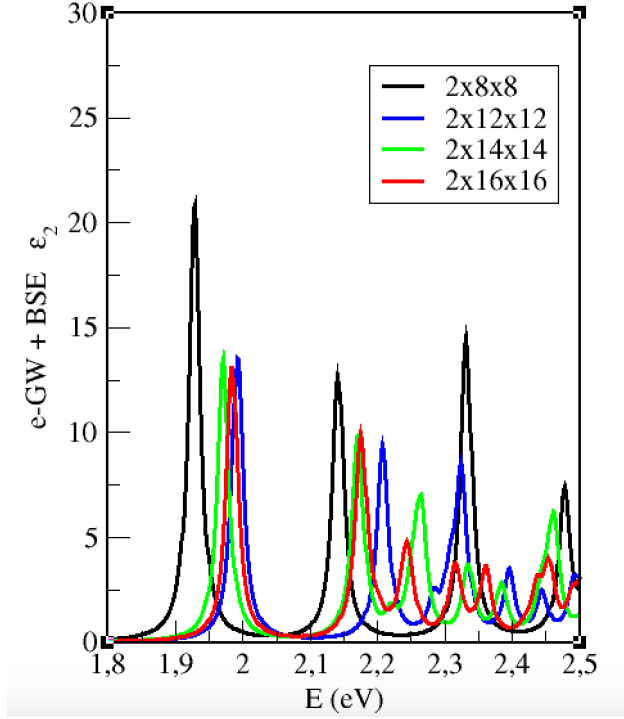


Figure S2: Convergence of the BSE spectrum as function of the k -point mesh employed for sampling the Brillouin.

8.403 Å, $b=8.664$ Å, $c=17.073$ Å, $\alpha=94.51^\circ$, $\beta=100.87^\circ$, $\gamma=90.05^\circ$. We select such system to later perform the Many-Body excited-state analysis. For the sake of comparison, we also calculated a single-layer structure for the Pb-based counterpart, which is obtained halving the cell along the c axis in the bilayer of $(\text{PEA})_2\text{PbI}_4$ reported in Ref. 3. In our calculations the parameters are $a=8.7389$ Å, $b=8.7403$ Å, $c=16.9195$ Å, $\alpha=79.52^\circ$, $\beta=79.53^\circ$, $\gamma=89.64^\circ$. On top of such optimized structures we preliminary calculate bands and Density of States (DOS). While PAW/PBE-D3 including relativistic effects are reported in the main text, here we show, in order to highlight the impact of their inclusion, the same bandstructures without SOC (see Fig.S1).

We verified that residual forces are < 0.02 eV/Å and that the final atomic positions were very similar to the initial ones. In the QE relaxation simulations a kinetic energy cutoff of 2176 eV is needed by using norm-conserving pseudopotentials.¹¹ On top of fully relaxed atomic structures we perform self and non-self consistent DFT calculations at different k -

points grids to have the possibility to check the convergence in the k-BZ sampling at GW and BSE level of calculation. The many-body code YAMBO^{12,13} is then used to obtain the quasi-particle (QP) energies in the GW approximation and the optical excitation energies and spectra solving the Bethe–Salpeter Equation (BSE).^{14–18} For the GW simulations a plasmon–pole approximation for the inverse dielectric matrix is applied,¹⁹ 163 eV (1088 eV) are used for the correlation, Σ_c , (exchange, Σ_x) part of the self-energy and the sum over the unoccupied states for Σ_c and the dielectric matrix is performed up to $\simeq 20$ eV above the VBM. Several works have shown the importance of self-consistency in the GW approach for several classes of compounds.^{20–24} In particular, Filip *et al.* in ref. 25, have shown that doing a partial self-consistent cycle by updating only the energies both in G and W ($evGW$), is enough to obtain a good agreement with experimental electronic gaps of several perovskites, mitigating the dependency of the starting point present in the G_0W_0 approximation. Recently we had a similar positive experience in layered and $\text{Cs}_2\text{Au}_2\text{I}_6$ double perovskites.²³ For this reason we use here the same self-consistent GW approach, noticing an increase of the gap of about 0.5 eV from G_0W_0 to the third iteration where convergence is reached. The Bethe-Salpeter equation has been solved within the Tamm-Dancoff^{18,26} approximation (which is generally valid for bulk compounds to describe neutral excitations well below the plasma frequency of the material) and fully taking into account the spinorial nature of the wavefunctions. 4 occupied and 4 unoccupied states have been used in the excitonic Hamiltonian. It is worth pointing out that in the BSE calculations the energies are the QP ones at the end of the self-consistent cycle and the static part of the screening used to build up the correlation part of the excitonic kernel is calculated at the same level of self-consistency. The convergence in the k -sampling for the BSE calculations has been checked for a smaller 1x1 cell. Figure S2 shows the optical spectra for the Sn-based perovskite obtained with several k -grids.

Table 1

B.E.	(PEA) ₂ SnI ₄ (stacked)	(PEA) ₂ SnI ₄ (monolayer)	(PEA) ₂ PbI ₄ (monolayer)
<i>VBM</i>	$I_{eq}(5p_x + 5p_y) = 42.7\%$ $I_{ap}(5p_z) = 12.2\%$ Sn (5s)=38.4%	$I_{eq}(5p_x + 5p_y) = 47.8\%$ $I_{ap}(5p_z) = 6.55\%$ Sn (5s)=38.2%	$I_{eq}(5p_x + 5p_y) = 53.2\%$ $I_{ap}(5p_z) = 16.0\%$ Pb (6s)=28.9%
<i>CBM</i>	Sn (5p _x + 5p _y) = 75.4% $I_{eq}(5s)=8.35\%$	Sn (5p _x + 5p _y) = 75.0% $I_{eq}(5s)=8.0\%$	Γ point: Pb (6p _x + 6p _y) = 72.2% (traces of I 5s,5p orbitals) L point: Pb (6p _x + 6p _y) = 73.0% (traces of I 5s,5p orbitals)

Assignment of transient absorption features at 5 K

The transient absorption spectrum of $(\text{PEA})_2\text{SnI}_4$ is very rich and composed of multiple overlapping features. In particular we can identify five PB features, labelled Γ_1 to Γ_5 , two PIA features called Π_1 and Π_1^* , and a stimulated emission peak Φ_1 . The main features related to the dynamics of X_{LE} , X_{HE_1} and X_{HE_2} are Γ_1 , Γ_1^* , Γ_4 and Γ_5 , which are discussed in depth in this manuscript.

On the red edge of Γ_1 there are two PA bands, Π_1 and Π_1^* and another positive $\Delta T/T$, labelled Φ . Due to the absence of any feature either in the calculated or experimentally measured linear absorption spectra and to the presence of a photoluminescence (PL) (fig. S3) band at the energy of Φ , we assign it to SE. Conversely, the well defined Π_1 feature is associated to the exciton \rightarrow biexciton transition.²⁷

We also observe a broad featureless negative band extending from 1.97 eV to 2.2 eV, where no excitonic features are expected to be found, which is typically associated to the photo-induced changes in the refractive index across the entire spectrum.²⁸ Atop this broad negative feature, we may identify two "positive-going" features at 2.02 eV and 2.13 eV, more prominent for the high energy excitation, with associated low oscillator strength resonances in the linear spectrum: accordingly, we identify overlapping PB bands Γ_2 and Γ_3 at those energies. In the spectral region corresponding to X_{HE} the most prominent bleach features are found at Γ_4 and Γ_5 : the decay of the relative intensity of Γ_5 gives indication of the transfer of the cooling of the population of X_{HE_2} toward X_{LE} . The relative intensity of Γ_4 to Γ_1 on the other hand increases at longer delays: this is a consequence of the transfer of population within the exciton fine structure at X_{LE} and possibly to the states with lower oscillator strength, predicted a few meV before the main peak at X_{LE} by our theoretical analysis.

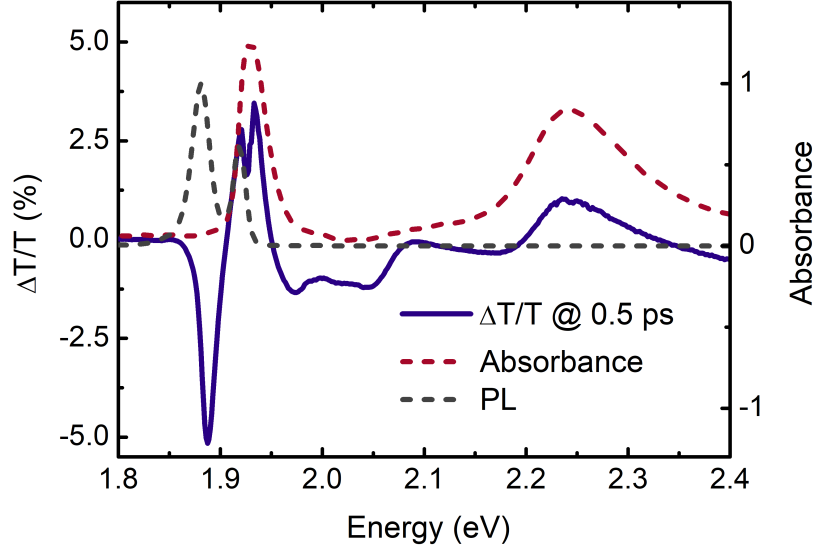


Figure S3: Comparison between the lineshape of differential transmission at a pump delay of 0.5 ps (solid blue line), the static optical absorbance (dashed red line) and the static photoluminescence (dashed grey line). The $\Delta T/T$ feature at 1.92 eV, identified as Γ_1 , matches the photoluminescence peak, while Γ_1^* corresponds to the maximum of static absorbance. All data is measured at a temperature of 25 K.

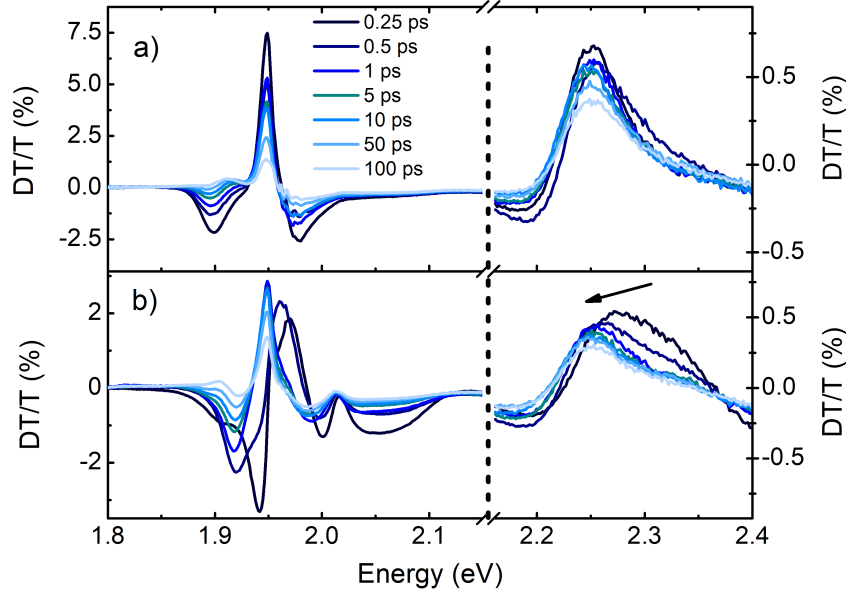


Figure S4: Unnormalized differential transmission spectra of $(\text{PEA})_2\text{SnI}_4$ upon (a),(b) resonant excitation ($E_{\text{pump}} = 1.96$ eV) of the lowest lying excitonic states (c),(d) non-resonant excitation of hot free carriers ($E_{\text{pump}} = 3.1$ eV). All experiments were performed at 77 K and with a pump fluence of $350 \mu\text{W}/\text{cm}^2$.

Full temperature dependent transient absorption data

Transient absorption spectra were collected in a temperature range from 5 K to 295 K. All the temperature-dependent results discussed in this work were collected using a 490 nm pump with an intensity of $0.5 \mu\text{W}$.

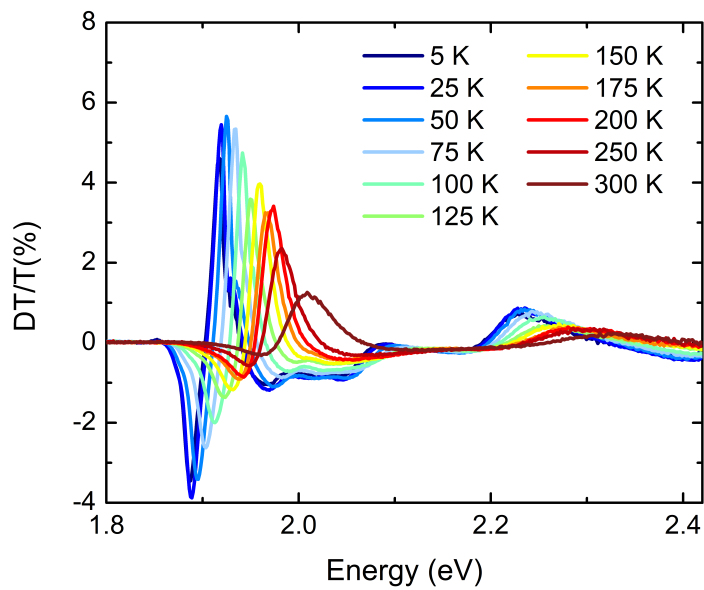


Figure S5: Differential transmission spectra at a pump delay $\tau = 1$ ps for temperatures between 5 K and 300 K

Details of DT fit modeling

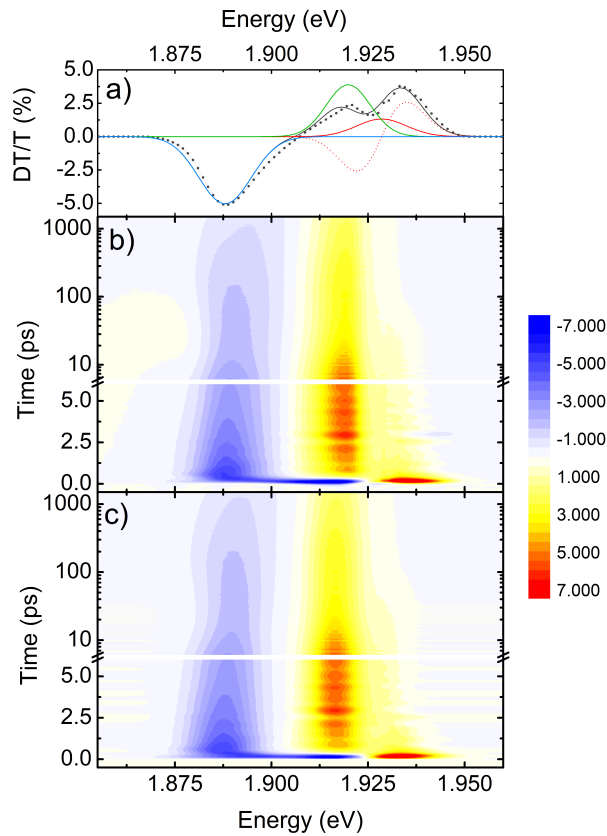


Figure S6: Fit result for the $T = 5$ K map. a) Synthetic view of the model as discussed in the main text (Exciton bleach in red, PIA in blue, SE in green): the data at 1 ps delay (black circles) is well reproduced by the fit (solid black line). b) 2D map of the TA signal in the region of the largest excitonic features. c) 2D map generated by the fit, showing excellent agreement with the measured data up to a delay $\tau = 1.2$ ns.

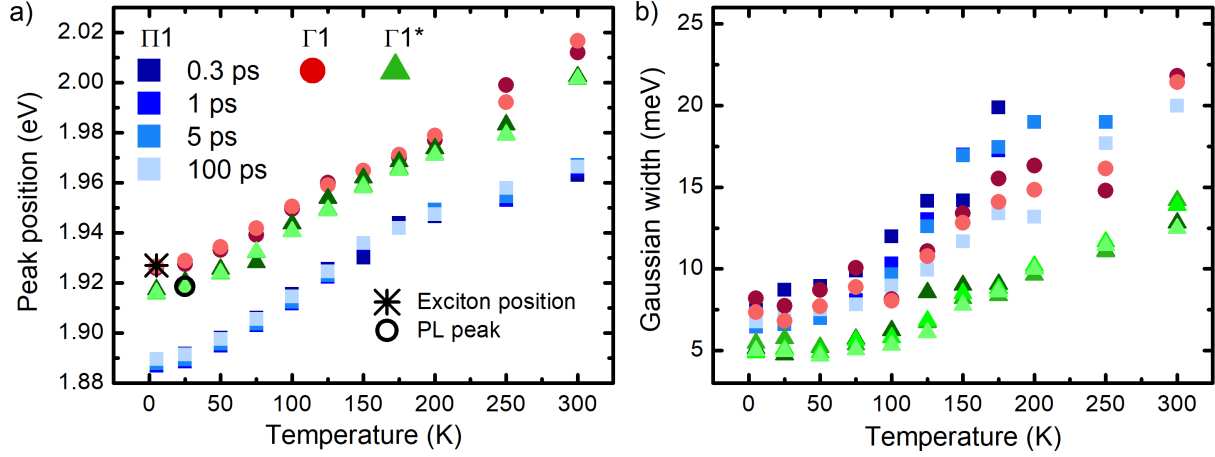


Figure S7: Values of the estimated a) peak position and b) width of fit components as a function of pump delay τ .

A model was developed to fit the temporal evolution of the excitonic peak X1 at all temperatures using a minimal number of components. The model is comprised of three gaussian peaks representing respectively the excitonic bleach Γ_1^* , photoinduced absorption Π , and the stimulated emission Γ_1 , as well as a gaussian 1st derivative shape $d\Gamma$ representing a spectral shift of the exciton bleach.

Altogether, the differential transmission is written as $\Delta T(T, \tau) = \Gamma_1^* + d\Gamma_1^* + \Gamma_1 + \Pi$ with:

$$\Gamma_1^* = A_{\Gamma_1^*} \exp(-(E - \mu_{\Gamma_1^*})^2 / 2\sigma_{\Gamma_1^*}^2) \quad (1)$$

$$d\Gamma = A_{d\Gamma} (E - \mu_{\Gamma_1^*}) / \sigma_{\Gamma_1^*}^2 \exp(-(E - \mu_{\Gamma_1^*})^2 / 2\sigma_{\Gamma_1^*}^2) \quad (2)$$

$$\Pi = -A_{\Pi} \exp(-(E - \mu_{\Pi})^2 / 2\sigma_{\Pi}^2) \quad (3)$$

$$\Gamma_1 = A_{\Gamma_1} \exp(-(E - \mu_{\Gamma_1})^2 / 2\sigma_{\Gamma_1}^2) \quad (4)$$

Since the derivative lineshape reflects the shift of the excitonic bleach component Γ_1^* , it has the same width and peak position. The spectral shift of the exciton bleach is related

to band gap renormalization and excitonic screening: it reflects early dynamics upon the formation of an excitonic population. As such, the derivative shape component was removed from the model for times longer than 15 ps: however, its amplitude $A_{d\Gamma}$ naturally reduced to zero on faster timescales than allowed. To ensure smooth changes in the fit parameters, even in presence of closely spaced features involving opposing contribution (e.g. positive and negative gaussian components), a regularization condition was imposed on the peak position and width of the gaussian features, only allowing numerical variations up to $\pm 50\%$ of the results at the previous delay.

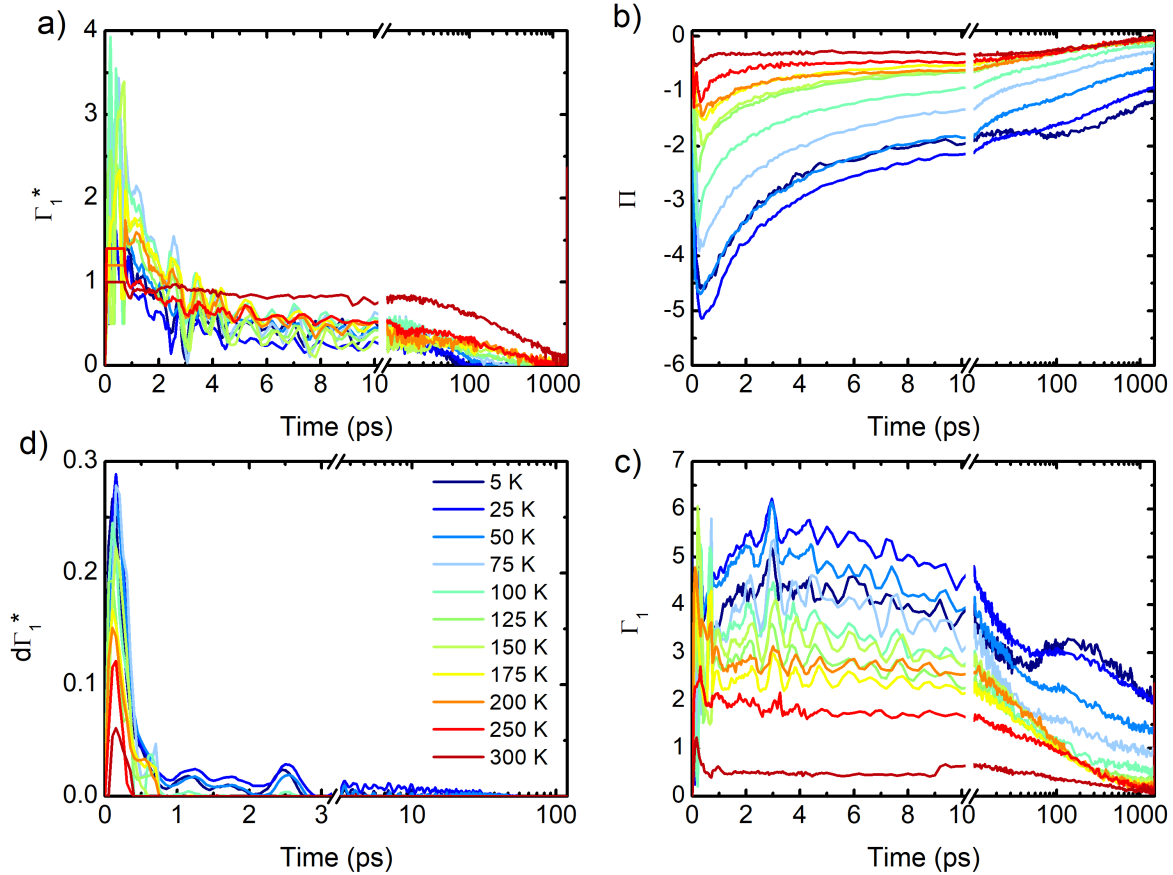


Figure S8: Amplitudes of the different fit components as a function of τ for all temperatures. a) Exciton bleach Γ_1^* b) Photoinduced absorption Π c) Stimulated emission Γ_1 d) Derivative lineshape $d\Gamma_1^*$ (corresponding to the shift of Γ_1^*). The 90° out of phase oscillations appearing in a) and c) stem from the observed coherent phonons.

Using this model, excellent agreement between fit and experimental data could be achieved at all temperatures: experimental data and fit results are compared for $T = 5$ K in fig.S6. The temporal evolution of fit parameters at all temperatures is shown in fig.S8, S7. Strikingly, Γ_1 dominates over Γ_1^* for all temperatures up to 250 K.

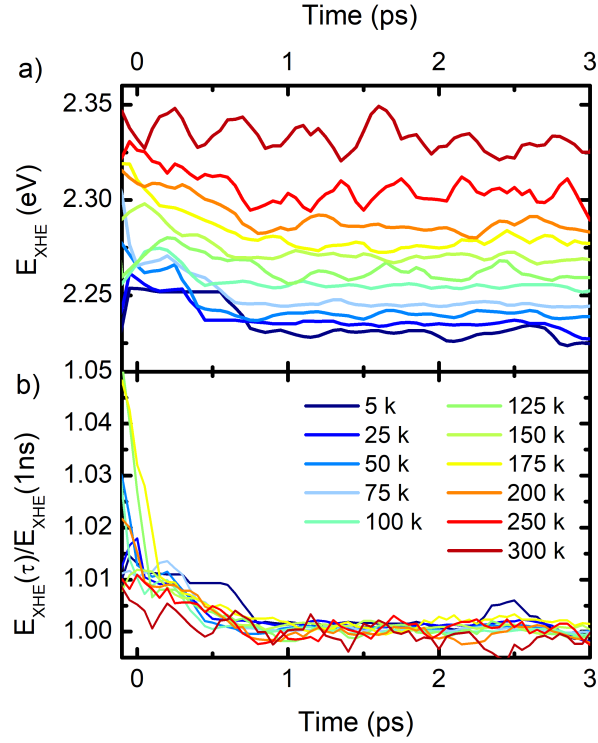


Figure S9: Temperature dependent fingerprint of thermalization. a) spectral position of the X_{HE} peak for all temperatures. b) Figure of merit for thermalization time: ratio between the time dependent X_{HE} position $E_{peak}(t)$ to the stabilized X_{HE} position at τ delays, $E_{peak}(1 ns)$

DT measurement stability

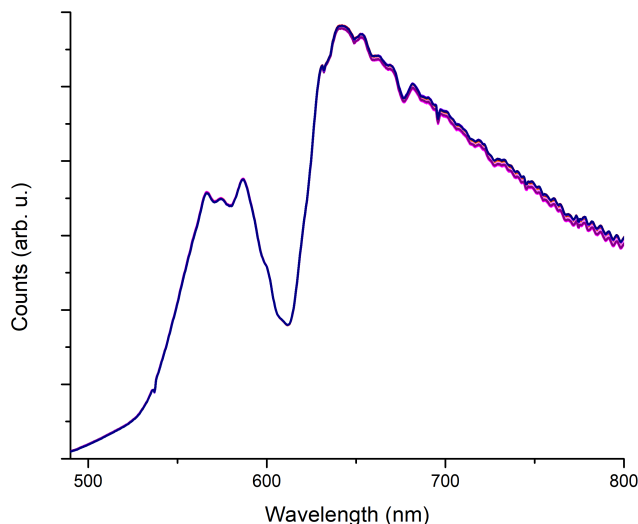


Figure S10: White light probe as transmitted through the sample over each of 10 scans (approximately 30 minutes) at 300 K, $350 \mu\text{W}/\text{cm}^2$ pump fluence.

References

- (1) Zhang, T.; Zhou, C.; Feng, X.; Dong, N.; Chen, H.; Chen, X.; Zhang, L.; Lin, J.; Wang, J. Regulation of the luminescence mechanism of two-dimensional tin halide perovskites. *Nature communications* **2022**, *13*, 1–11.
- (2) Sheikh, T.; Nawale, V.; Pathoor, N.; Phadnis, C.; Chowdhury, A.; Nag, A. Molecular intercalation and electronic two dimensionality in layered hybrid perovskites. *Angewandte Chemie* **2020**, *132*, 11750–11756.
- (3) Du, K.-z.; Tu, Q.; Zhang, X.; Han, Q.; Liu, J.; Zauscher, S.; Mitzi, D. B. Two-dimensional lead (II) halide-based hybrid perovskites templated by acene alkylamines: crystal structures, optical properties, and piezoelectricity. *Inorganic chemistry* **2017**, *56*, 9291–9302.

- (4) Kresse, G.; Hafner, J. Ab initio molecular dynamics for open-shell transition metals. *Phys. Rev. B* **1993**, *48*, 13115–13118.
- (5) Kresse, G.; Hafner, J. Ab initio molecular-dynamics simulation of the liquid-metal–amorphous–semiconductor transition in germanium. *Phys. Rev. B* **1994**, *49*, 14251–14269.
- (6) Kresse, G.; Furthmüller, J. Efficiency of ab-initio total energy calculations for metals and semiconductors using a plane-wave basis set. *Comput. Mater. Sci.* **1996**, *6*, 15 – 50.
- (7) Kresse, G.; Furthmüller, J. Efficient iterative schemes for ab initio total-energy calculations using a plane-wave basis set. *Phys. Rev. B* **1996**, *54*, 11169–11186.
- (8) Perdew, J. P.; Burke, K.; Ernzerhof, M. Generalized gradient approximation made simple. *Phys. Rev. Lett.* **1996**, *77*, 3865–3868.
- (9) Blöchl, P. Projector augmented-wave method. *Phys. Rev. B* **1994**, *50*, 17953–17979.
- (10) Kresse, G.; Joubert, D. From ultrasoft pseudopotentials to the projector augmented-wave method. *Phys. Rev. B* **1999**, *59*, 1758–1775.
- (11) Van Setten, M.; Giantomassi, M.; Bousquet, E.; Verstraete, M. J.; Hamann, D. R.; Gonze, X.; Rignanese, G.-M. The PseudoDojo: Training and grading a 85 element optimized norm-conserving pseudopotential table. *Computer Physics Communications* **2018**, *226*, 39–54.
- (12) Marini, A.; Hogan, C.; Grüning, M.; Varsano, D. Yambo: An ab initio tool for excited state calculations. *Comp. Phys. Comm.* **2009**, *180*, 1392 – 1403.
- (13) Sangalli, D. et al. Many-body perturbation theory calculations using the yambo code. *J. Phys. Condens. Matter* **2019**, *31*, 325902.

- (14) Strinati, G.; Mattausch, H. J.; Hanke, W. Dynamical aspects of correlation corrections in a covalent crystal. *Phys. Rev. B* **1982**, *25*, 2867–2888.
- (15) Strinati, G. Application of the Green's functions method to the study of the optical properties of semiconductors. *La Rivista del Nuovo Cimento (1978-1999)* **1988**, *11*, 1–86.
- (16) Hanke, W.; Sham, L. J. Dielectric Response in the Wannier Representation: Application to the Optical Spectrum of Diamond. *Phys. Rev. Lett.* **1974**, *33*, 582–585.
- (17) Hanke, W.; Sham, L. J. Many-particle effects in the optical spectrum of a semiconductor. *Phys. Rev. B* **1980**, *21*, 4656–4673.
- (18) Onida, G.; Reining, L.; Rubio, A. Electronic excitations: density-functional versus many-body Green's-function approaches. *Reviews of modern physics* **2002**, *74*, 601.
- (19) Godby, R.; Needs, R. Metal-insulator transition in Kohn-Sham theory and quasiparticle theory. *Phys. Rev. Lett.* **1989**, *62*, 1169.
- (20) Sarsari, I. A.; Pemmaraju, C.; Salamati, H.; Sanvito, S. Many-body quasiparticle spectrum of Co-doped ZnO: A G W perspective. *Phys. Rev. B* **2013**, *87*, 245118.
- (21) Umari, P.; Mosconi, E.; De Angelis, F. Relativistic GW calculations on $\text{CH}_3\text{NH}_3\text{PbI}_3$ and $\text{CH}_3\text{NH}_3\text{SnI}_3$ perovskites for solar cell applications. *Sci. Rep.* **2014**, *4*, 1–7.
- (22) Giorgi, G.; Van Schilfgaarde, M.; Korkin, A.; Yamashita, K. On the Chemical Origin of the Gap Bowing in $(\text{GaAs})_{1-x}\text{Ge}_2\text{x}$ Alloys: A Combined DFT-QS GW Study. *Nanoscale Res. Lett.* **2010**, *5*, 469–477.
- (23) Giorgi, G.; Yamashita, K.; Palummo, M. Two-dimensional optical excitations in the mixed-valence $\text{Cs}_2\text{Au}_2\text{I}_6$ fully inorganic double perovskite. *J. Mater. Chem. C* **2018**, *6*, 10197–10201.

- (24) Palummo, M.; Berrios, E.; Varsano, D.; Giorgi, G. Optical properties of lead-free double perovskites by ab initio excited-state methods. *ACS Energy Lett.* **2020**, *5*, 457–463.
- (25) Filip, M. R.; Giustino, F. G W quasiparticle band gap of the hybrid organic-inorganic perovskite $\text{CH}_3\text{NH}_3\text{PbI}_3$: Effect of spin-orbit interaction, semicore electrons, and self-consistency. *Phys. Rev. B* **2014**, *90*, 245145.
- (26) Dancoff, S. Non-adiabatic meson theory of nuclear forces. *Physical Review* **1950**, *78*, 382.
- (27) Thouin, F.; Neutzner, S.; Cortecchia, D.; Dragomir, V. A.; Soci, C.; Salim, T.; Lam, Y. M.; Leonelli, R.; Petrozza, A.; Srimath Kandada, A. R., et al. Stable biexcitons in two-dimensional metal-halide perovskites with strong dynamic lattice disorder. *Phys. Rev. Mater.* **2018**, *2*, 034001.
- (28) Price, M. B.; Butkus, J.; Jellicoe, T. C.; Sadhanala, A.; Briane, A.; Halpert, J. E.; Broch, K.; Hodgkiss, J. M.; Friend, R. H.; Deschler, F. Hot-carrier cooling and photoinduced refractive index changes in organic-inorganic lead halide perovskites. *Nature communications* **2015**, *6*, 1–8.